

Review

High Field Single- to Few-Cycle THz Generation with Lithium Niobate

Xing Zhu, David R. Bacon, Julien Madéo and Keshav M. Dani *

Femtosecond Spectroscopy Unit, Okinawa Institute of Science and Technology Graduate University, 1919-1 Tancha, Onna, Okinawa 904-0495, Japan; xing.zhu1@oist.jp (X.Z.); david.bacon@oist.jp (D.R.B.); julien.madeo@oist.jp (J.M.)

* Correspondence: kmdani@oist.jp

Abstract: The transient terahertz (THz) pulse with high peak field has become an important tool for matter manipulation, enabling many applications such as nonlinear spectroscopy, particle acceleration, and high harmonic generation. Among the widely used THz generation techniques, optical rectification in lithium niobate (LN) has emerged as a powerful method to achieve high fields at low THz frequencies, suitable to exploring novel nonlinear phenomena in condensed matter systems. In this review, we focus on introducing single- to few-cycle THz generation in LN, including the basic principles, techniques, latest developments, and current limitations. We will first discuss the phase matching requirements of LN, which leads to Cherenkov-like radiation, and the tilted pulse front (TPF) technique. Emphasis will be put on the TPF technique, which has been shown to improve THz generation efficiency, but still has many limitations. Different geometries used to produce continuous and discrete TPF will be systematically discussed. We summarize the advantages and limitations of current techniques and future trends.

Keywords: terahertz radiation; lithium niobate; tilted pulse front



Citation: Zhu, X.; Bacon, D.R.; Madéo, J.; Dani, K.M. High Field Single- to Few-Cycle THz Generation with Lithium Niobate. *Photonics* **2021**, *8*, 183. <https://doi.org/10.3390/photonics8060183>

Received: 5 April 2021
Accepted: 17 May 2021
Published: 24 May 2021

Publisher's Note: MDPI stays neutral with regard to jurisdictional claims in published maps and institutional affiliations.



Copyright: © 2021 by the authors. Licensee MDPI, Basel, Switzerland. This article is an open access article distributed under the terms and conditions of the Creative Commons Attribution (CC BY) license (<https://creativecommons.org/licenses/by/4.0/>).

1. Introduction to High Field

Terahertz (THz) radiation, at the junction between traditional electronics and optics, has attracted intense research interest due to its fascinating applications in physics, chemistry, and biology. It is widely used as a spectroscopic tool that provides a unique probe for low energy excitations such as lattice vibration [1], exciton transition [2], charge carrier motion [3], and spin excitation [4]. Recent advances in generation techniques have provided access to transient THz pulses with peak fields exceeding the MV/cm range using tabletop setups. This intense THz radiation has enabled new applications in the manipulation of matter over picosecond timescales. On one hand, the excitation of low-energy states has provided the ability to distort the lattice structure [5,6], to switch ferroelectric polarization [7], and to non-adiabatically quench superconductivity [8]. On the other hand, high fields can provide significant ponderomotive energy, far exceeding that of the THz photon energy. This non-resonant excitation has been applied for free particle acceleration [9], high-harmonic generation [10], and impact ionization in semiconductors [11]. In addition to the strong Coulomb force from the electric field, the corresponding magnetic field (0.33 T for 1 MV/cm) also provides a significant Zeeman interaction, enabling the direct control of magnetism at an ultrafast timescale [12]. The picosecond pulse can be further used in combination with traditional scanning tunneling microscopes [13,14] or angle resolved photoemission spectroscopy [15], allowing one to directly observe the ultrafast dynamics of low-energy excited states and nonlinear phenomena in condensed matter systems.

Different applications and studies require various types of THz sources with peak electrical field ranging from kV/cm to MV/cm. Transient THz pulses with relatively low-frequency components ranging from sub- to few-THz, are particularly applicable in condensed matter physics. For instance, the resonant excitation of many quasi-particle

states and collective excitations, such as exciton fine structure, superconductor gaps, and molecular motion, specifically require the use of a relatively narrow band excitation centered around 1 THz (4 meV) [16–18]. Furthermore, for non-resonant excitations, ponderomotive energy has an inverse-square dependence on pump frequency, which means that a low-frequency THz pulse has the significant advantage of providing larger ponderomotive potential.

Various tabletop techniques have been studied to achieve high fields in the THz range, such as photoconductive antennas, optical rectification (OR) in nonlinear crystals, dual-color air plasma and spintronic emitters, as shown in Figure 1a. Photoconductive antennas (PCA) generate THz radiation below 3 THz with a high signal-to-noise ratio, but the generated fields are limited by dielectric breakdown and saturation effects. Nonetheless, recent efforts have led to peak fields up to hundreds of kV/cm by large-aperture PCA (LAPCA) [19]. Another approach is the use of nonlinear processes such as OR in inorganic semiconductors, e.g., ZnTe and GaP, which, due to their low electro-optic coefficients and low saturation thresholds, have not demonstrated THz field larger than 0.6 MV/cm [20]. Organic crystals, including DSTMS, OH1, and DAST have shown the ability to generate high-field THz (83 MV/cm) with very high efficiencies exceeding 1%, benefiting from their large nonlinear coefficients [21]. However, at low frequencies, THz generation in organic materials is limited by strong phonon absorptions [22]. Additionally, their relatively low damage threshold, material degradation in ambient conditions, and small crystal size hinders their use for wider applications. Recently, dual-color air plasma, with a virtually unlimited damage threshold, has been used to achieve a record high THz field above 100 MV/cm [23]. Such high fields have been generated via the use of a mid-infrared pump instead of the typical 800 nm pump which had so far been limited to creating a field of up to 8 MV/cm [24]. Compared to OR in organic materials, air plasma THz generation provides even more spectral bandwidth and higher frequency components. Finally, the spintronic emitter, as an emerging method, has demonstrated fields up to 300 kV/cm but the generated THz displays a broadband spectrum and a relatively low conversion efficiency ($<10^{-6}$). Among all these techniques, lithium niobate (LN) has been shown to be an efficient method of generating high field THz up to the MV/cm level while providing a narrow spectrum at low frequencies, making it suitable for the applications described above.

Because of these unique properties, there have been enormous efforts within the community to develop intense THz pulses using LN crystals. The first demonstration of THz generation from LN used picosecond laser excitation in 1971 [25]. Hebling et al. first proposed the tilted pulse front (TPF) technique for THz generation in 2002 [26], and it was experimentally realized in LN one year later [27]. Later extensive theoretical and experimental research have been carried out to improve generation efficiency and to scale up THz pulse energy and field intensity, as listed in Figure 1b. Currently, the conversion efficiency can reach as high as 3.8% using a 1.03 μm pump and a cryogenically cooled crystal to reduce absorption [28]. The peak field record was established at 1.2 MV/cm with a kHz system [29], while the output THz pulse energy can reach mJ levels using 10 Hz laser system [30,31]. In the following, we focus on single- to few-cycle THz generation from LN, i.e., single- to few-periods of the generated field at the central frequency. The next sections are organized as follows: in Section 2, we introduce the basic principle for achieving phase matching for THz generation in LN. Then, THz generation through Cherenkov-like radiation geometry with many novel designs are summarized. Next, we emphasize the TPF method as it is the key breakthrough to achieving intense THz generation. The principle of TPF techniques will be analyzed, followed by a detailed discussion of detrimental factors, optimization methods, and latest developments. Section 4 introduces the discrete TPF method with the latest progress. The last section will summarize developments and future directions.

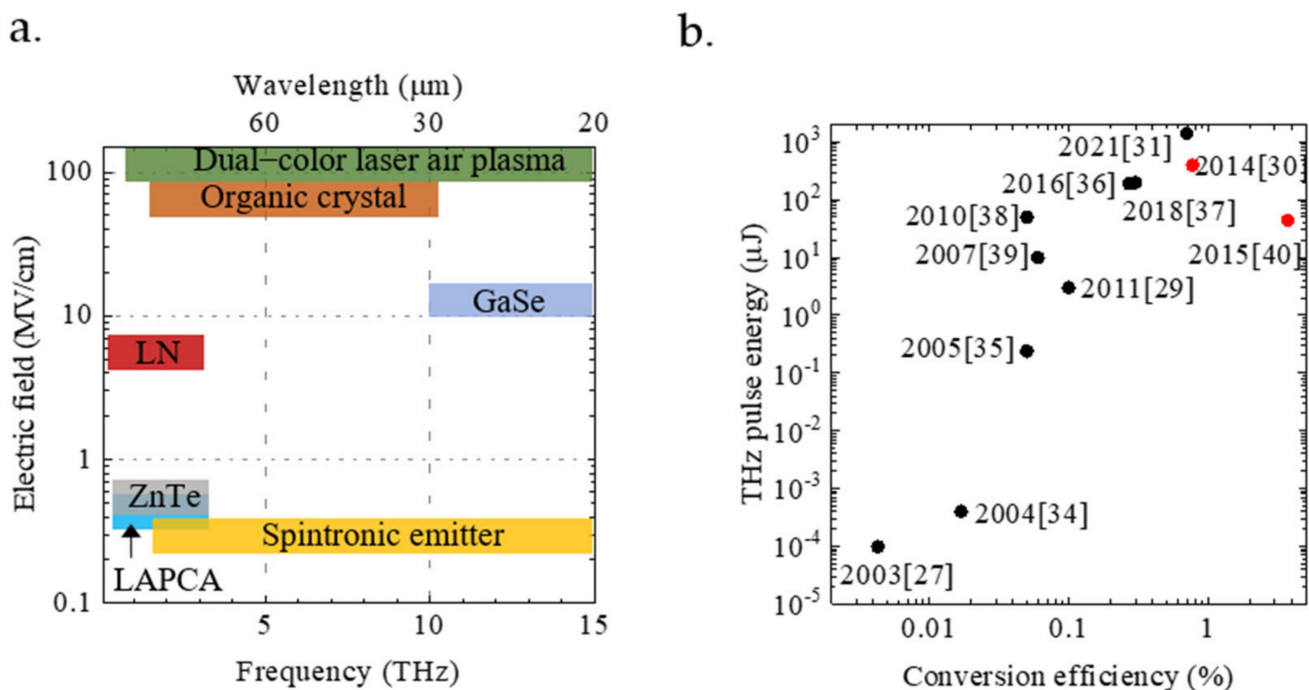


Figure 1. (a) Methods to generate high-field THz. The peak field records and typical outputted spectrum are listed for different conventional methods. Dual-color laser air plasma: 100 MV/cm [23] for 1–20 THz; organic crystal: 83 MV/cm [21] for 1–10 THz; GaSe: 12 MV/cm [32] for 10–40 THz; spintronic emitter: 300 kV/cm [33] for 1–30 THz; LAPCA: 330 kV/cm for 0.1–3 THz; ZnTe: 570 kV/cm for 0.1–3 THz [20]; LN: 6.3 MV/cm [31] for 0.1–3 THz. (b) Development of THz generation from LN with TPF techniques over the years [27,29–31,34–40]. The black dots represent 800 nm pump and the red dots represent 1030 nm pump.

2. The Cherenkov Geometry

In linear optics or at relatively low field intensities, the induced polarization of a medium can be said to have a linear relationship with the electric field transmitted through it. Indeed, the polarization of a material can be described by the following series: $P = \chi^{(1)}E + \chi^{(2)}EE + \dots$, where $\chi^{(n)}$ is the n th-order susceptibility tensor. In non-linear optics, higher order terms become significant, as the polarization becomes non-linear with the electric field. As a second-order nonlinear effect, OR generates quasi-DC polarization when a femtosecond laser pulse passes the nonlinear material. This induced polarization is proportional to the envelope of the incident optical pulse. Previously, OR has been widely used for THz generation in multiple types of materials, such as inorganic semiconductors, and organic materials. The ferroelectric crystal LN has become attractive for intense THz generation owing to several advantages it has over other crystals. The first reason is the large effective $\chi^{(2)}$ nonlinear coefficient of OR ($d_{eff} \sim 168$ pm/V). As a comparison, this coefficient is significantly greater than that of typical semiconductors used for OR, such as ZnTe (~ 68 pm/V), GaSe (~ 28 pm/V), and GaP (~ 25 pm/V) [41]. In addition, the wide bandgap of LN (3.8 eV at room temperature) limits multiphoton absorption, suppressing THz absorption by free carriers under high pump fluence [33]. For example, in a material with low defect densities, only 4-photon absorption is possible under 1030 nm excitation, and 3-photon absorption for an 800 nm excitation, although 2-photon absorption can be induced by impurities [41–44].

In practice, one must overcome several problems to use LN for efficient THz generation. First, the photorefractive effect in LN, i.e., the pump-induced change of the refractive index, can lead to beam distortion and, at high fluence, can induce damage to the crystal, although this phenomenon can be largely reduced by MgO doping [45,46]. Next, OR requires velocity matching of the pump and the THz wave, as they both propagate through the material: $v_{vis}^{sr} = v_{THz}^{ph}$, where v_{vis}^{sr} is the group velocity of the pump and v_{THz}^{ph} is the

phase velocity of the generated THz wave. However, the refractive index of LN in the THz region ($n_e \sim 5$) is more than two times higher than it is in visible regime ($n_e \sim 2.2$), which means that the THz generated travels much slower than the visible excitation pulse.

The simplest way to achieve phase matching in LN is through the use of a Cherenkov geometry. When the pump is focused with a narrow beam waist, THz radiation can be produced through the electro-optic Cherenkov effect [26,47]. The propagating THz radiation forms a cone with a Cherenkov angle $\theta_c = \cos^{-1} \left(\frac{v_{THz}^{ph}}{v_{vis}^{gr}} \right)$, as shown in Figure 3a. In order to make the generated THz and optical pump interfere constructively, the excitation beam waist within the LN crystal must be smaller than the THz wavelength, which is around 60 μm at 1 THz in LN. We note that a tighter focus also brings more high frequency components [48]. In addition to the use of a point source for the pump, a line source has also been proposed [49]. This technique employs a cylindrical lens which allows one to increase the total excitation energy by increasing the cross-section of the focus, while keeping the fluence below the damage threshold. In this configuration, the excitation beam is aligned along the slab edge of the crystal and the THz radiates into a wedge, as shown in Figure 3b. However, in this configuration, the generated THz can be easily trapped inside the crystal because of its total internal reflections. One of the solutions to overcome this issue is to cut the LN with a special wedge angle to ensure that the THz wave exits perpendicularly to the surface. Total internal reflections can also be avoided by attaching a high-resistivity Si prism with low THz absorption to the emitting interface [48,50–52].

Instead of using a prism-type LN, other configurations consisting of embedding the LN crystal between two materials have been investigated to improve THz extraction. The first reported attempt was made with a cm-long, cm-wide and μm -thick LN slab sandwiched between a Si prism and a glass substrate, as shown in Figure 2a. This method reduces the THz beam path inside the LN and allows for a higher outcoupling efficiency [53]. However, only the THz radiation outputted from the Si prism was collected, while the residual radiation was absorbed by the glass substrate. Other studies have included the use of a Si-LN-Si [54] structure to couple the THz from both of the emitting surfaces, unfortunately proving impractical for most applications. To solve this issue, reflecting substrates such as metals were used to replace the glass substrate so that the THz pulse was reflected towards the side of the Si prism. In doing so, the generated THz spectrum becomes tunable by changing the air gap between LN and substrate [55,56] and it also displays a notch filtering effect as a consequence of the destructive interference between the direct and reflected components. Another recently proposed structure uses double-Si prisms with a special wedge angle, such that the THz radiation emitted on both sides experience total internal reflection within the prism and emits collinearly in free space [57]. Through continuous development over nearly two decades, the optical-to-THz conversion efficiency in LN employing Cherenkov geometry has improved from 1.75×10^{-5} to 1.3% [58,59]. However, in this simple focusing geometry, the pump pulse energy is usually limited to the μJ level, limiting the potential THz pulse energy to nanojoules and thus the field strength.

The Cherenkov geometry has two main shortcomings: firstly, the requirement for a narrow pump spot size limits the total excitation power on the crystal; secondly, this results in a strong divergence, making the generated THz challenging to collect. Meanwhile, to scale up the THz energy, the TPF method has been introduced as a way to meet the phase-matching requirements. Different from the Cherenkov geometry, TPF allows one to expand the pump spot size into two dimensions with an elliptical or circular cross section. Furthermore, the emitted THz exhibits a much better beam profile that is easier to collect and refocus. This has opened the possibility of increasing the pump energy, THz energy, and THz peak field, which will be discussed in the next section.

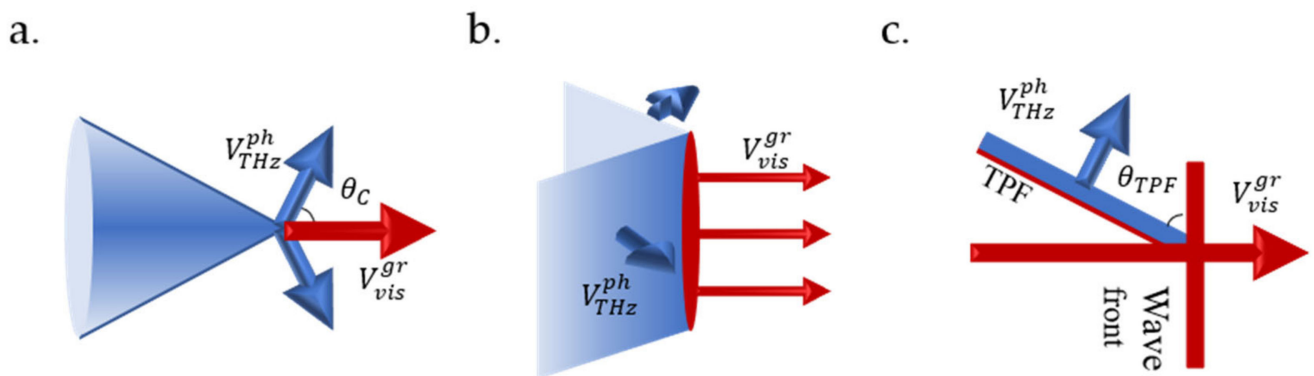


Figure 2. Experimental setup of Cherenkov geometry and the TPF technique. (a) Schematics of Cherenkov geometry. The Si prism couples the THz from thin-slab LN. (b) Schematics of the TPF technique. An intense femtosecond pump pulse is incident on the reflective grating with high groove density (1000–2000 lines/mm) and gets angularly dispersed. The optical axis of the LN crystal is perpendicular to the polarization from the grating with the highest reflection, so a half-wave plate is inserted to rotate the beam polarization. A double-lens telescope with 4f geometry is used to re-image the diffracted pump pulse in the LN crystal. (c) The spot size of THz generated from LN is magnified by the telescope, and then focused down by mirror. The THz field is detected by an EO sampling setup. [Reprinted/Adapted] with permission from [53] ©The Optical Society, and [29] ©AIP Publishing.

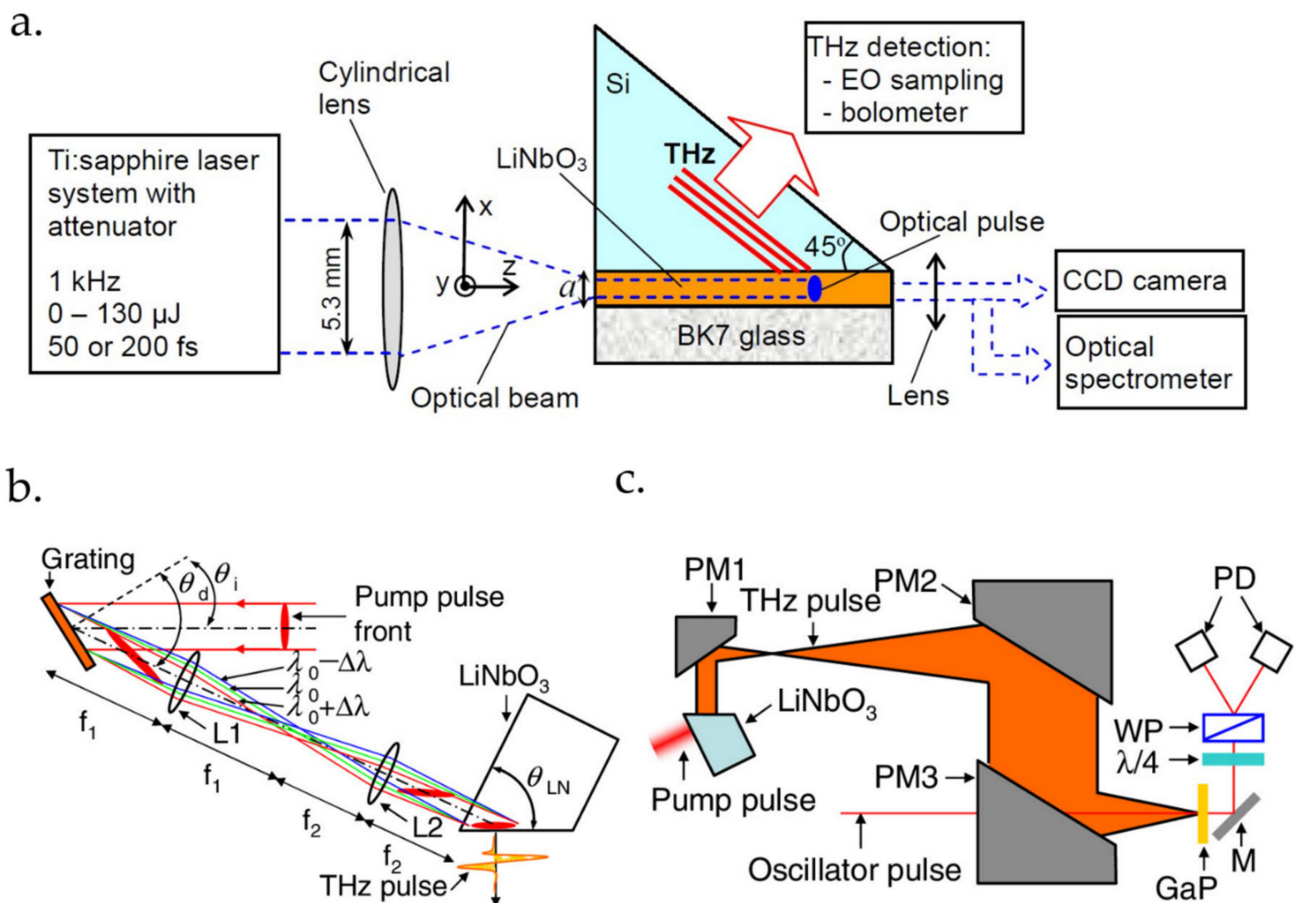


Figure 3. Cherenkov geometry and TPF. (a) The point focus beam radiates THz with Cherenkov angle θ_c , and the generated THz symmetrically forms a cone. (b) A side view for line focus. The THz radiates to two sides to form a wedge. (c) A top view of THz generation in the TPF technique, the THz wave radiates along with the propagation of the pump pulse front on one side.

3. TPF with a Grating

As shown in Figure 3c, when using the TPF technique, the front of the optical pulse experiences a tilt angle relative to the phase front, and normal to the propagation direction. If the tilt angle γ matches the Cherenkov angle $\gamma = \cos^{-1}\left(\frac{v_{\text{THz}}^{\text{ph}}}{v_{\text{vis}}^{\text{gr}}}\right) \sim 63^\circ$ for an 800 nm pump, the THz can propagate along with the pump pulse front and interfere constructively, since the phase matching condition is satisfied. In a conventional setup, a continuous TPF can be generated through the angular dispersion of a grating. Taking the reflective grating as an example, the incident angle θ_i and diffracted angle θ_d follow the grating equation $\sin \theta_i + \sin \theta_d = g\lambda$, where λ is the laser wavelength (usually 800 nm) and g is the groove density. The diffracted beam from the grating displays the angular dispersion $\frac{d\theta_d}{d\lambda} = \frac{g}{\cos \theta_d}$, which gives rise to a delay between different frequency components and leads to the TPF. The resulting tilt angle between the pulse front and the wave front induced by the grating in air is $\theta = \tan^{-1} \lambda \frac{d\theta_d}{d\lambda} = \tan^{-1} \left(\frac{g\lambda}{\cos \theta_d} \right)$ [60]. Furthermore, the angularly dispersed pulse needs to be accurately re-imaged in the LN crystal to meet the phase matching condition. However, for an 800 nm pump, a single grating with fewer than 2000 lines/mm is not enough to induce the required tilt angle of 63° to obtain phase matching. In addition, the large group refractive index of the pump within the crystal delays light propagation and compresses the dimensions of the TPF in the propagation direction, therefore reducing the tilt angle further. To overcome these issues, a lens or telescope acting on the dispersion plane with demagnification factor β is added after the grating to further increase the tilt angle. The final tilt angle for phase matching is given as $\theta = \tan^{-1} \left(\frac{g\lambda}{n_{\text{vis}}^{\text{gr}} \beta \cos \theta_d} \right)$ [29,42].

The ability to reimage the pump beam in the crystal critically influences THz generation efficiency and beam profile. The use of a single lens is the simplest geometry. However, it carries imaging errors such as spherical and chromatic aberrations. This results in imaging distortions on the crystal, causing a reduction of the peak intensity and a lack of image flatness, consequently causing a smaller spatial region in which phase matching is possible [42]. In this situation, the generated THz exhibits an asymmetric intensity profile and a strong divergence, making it difficult to collect and focus [61]. To optimize the geometry, a lens with longer focal length can produce a flatter grating image. A double-lens telescope can also significantly reduce the aberration, due to the compensation between two convex lenses [62]. In experiments with a double-lens setup, a nearly collimated THz beam can be generated with a divergence of around 50 mrad, close to the diffraction limit [27,29]. Another more direct method is to completely remove the optical imaging components using a contact-grating geometry, in which a transmissive or reflective grating is directly attached on the LN surface. This has been shown to eliminate any imaging error [63], making it suitable for higher input energy with a larger spot size. However, the realization of a contact grating with high groove density (>2000 lines/mm) is limited by either low diffraction efficiency or a complex fabrication process [64,65]. A reflective nonlinear slab (RNLS) using a high diffraction order was recently proposed to improve the diffraction efficiency and uniformity of THz generation after replacing the LN prism with a parallel slab [66,67]. In most applications, a double-lens telescope is still the most common method applied.

To improve the generation efficiency, the pump pulse duration and spectral bandwidth are important parameters to optimize. A longer Fourier-transform limited pulse duration displays a narrower spectral bandwidth, which is less sensitive to dispersion effects and provides longer effective THz generation length. Meanwhile, the lower peak intensity of a long pulse alleviates the detrimental effects at high pump fluence. However, too long a pulse duration results in long THz generation length, increasing absorption and reducing the intensity for efficient THz generation through OR. Calculations have predicted that the most efficient THz generation would be provided by Fourier-transform limited pulses of 300–500 fs at 800 nm pulse and 600 fs at 1 μm [42,44]. Experimentally, the record-high energy conversion efficiency for an 800 nm pump (0.35%) was observed when the pump

was tuned to a larger than 240 fs pulse duration [68]. A longer pulse of picosecond duration can still generate THz with over a two-times higher efficiency than that of 100 fs pulse [43]. The longer pulse duration also shifts the THz spectrum to a lower frequency with narrower bandwidth [42].

Multiple studies have investigated the use of short pulses as they are commonly accessible from the widely spread Ti:Sapphire lasers. Fourier-transform limited short pulses give broader bandwidth and are further spatially dispersed, so the imaging issues discussed above become more critical, and both the spherical and chromatic aberrations need to be carefully accounted for. For short pump pulse durations under 50 fs, replacing the lenses in the telescope with two concave mirrors has shown a significant reduction of the aberrations and an increase in the THz generation efficiency [62]. Alternative methods with a simpler geometry include cutting the laser spectrum [36] or chirping the pump pulse [37]. Both methods have been optimized to reach sub-mJ THz pulse energy and a conversion efficiency around 0.3%. Despite efforts to accommodate short-pulse laser systems, the use of short pulses exhibits limitations under high pump fluence, due to competing nonlinear effects, such as the cascading effect, self-phase modulation (SPM), and multiphoton absorption.

The cascading effect can enhance conversion efficiency at moderate pump fluence (several mJ/cm^2) but it can become detrimental at very high fluences. As a second-order nonlinear process, OR exhibits a quadratic dependence of the THz power on excitation power at a low fluence regime. However, a super-quadratic dependence occurs under a pump fluence of several mJ/cm^2 [49,69], due to the cascading effect [38,70,71]. The effect, which has been reported in other electro-optics crystals such as ZnTe [72], becomes more predominant in LN [39]. If the phase matching condition is satisfied, the optical pump photons can undergo repeated OR processes. The intense THz pulse modulates the phase of the pump pulse, resulting in its temporal compression, which further enhances the generation of high-frequency THz components and contributes to photon conversion exceeding the Manley–Rowe relation [69]. However, as the spectrum of the pump broadens with cascaded THz generation, the group velocity dispersion, from the angular dispersion (GVD-AD) and the materials dispersion (GVD-MD), becomes more significant, limiting further improvement of the conversion efficiency. At a very high pump fluence of over $10\text{s mJ}/\text{cm}^2$, these cascading effects, together with GVD-AD, become the major limiting factor, while the influence from the GVD-MD and the SPM contribution are less significant, as shown in Figure 4 [73]. Calculations including these cascading effects, GVD-AD, GVD-MD, and absorption predicted a 0.85% conversion efficiency, which is in reasonable agreement with most experiments [30].

In addition to these issues, absorption in LN is another obstacle for efficient THz generation. The absorption coefficient at room temperature is about 10 cm^{-1} in the THz region, but it can be reduced by one order of magnitude via cryogenic cooling [27,40]. When cooling with liquid nitrogen, the conversion efficiency has been reported to be more than double of that at room temperature [27,40] and the calculation has predicted that cooling down to 10 K can further improve performance [74]. It is worth noting that the generation setup requires re-optimization after cooling since material properties change significantly with temperature. As pump fluence increases the free carrier concentration, it leads to a stronger THz absorption. For an 800 nm pump, three-photon absorption plays an important role at high pump energy up to $50\text{ mJ}/\text{cm}^2$ [69]. Using a 1030 nm pump instead allows only 4-photon absorption, so the free carrier absorption is largely suppressed. Under a very high pump fluence of more than $50\text{ mJ}/\text{cm}^2$, the system needs delicate design, such as choosing a pump with the appropriate spectrum, pulse duration, group delay, and LN crystal under cooling, to suppress the saturation effects and prevent an efficiency decrease. With that in mind, a 1.4 mJ THz pulse has been demonstrated using a 214 mJ 800 nm pump pulse [31]. For a 1030 nm pump, the record-high efficiency reaches 3.8% at 150 K and 1.7% at room temperature [28,40] and the highest pulse energy reaches 0.4 mJ with a 0.77% energy conversion efficiency [30].

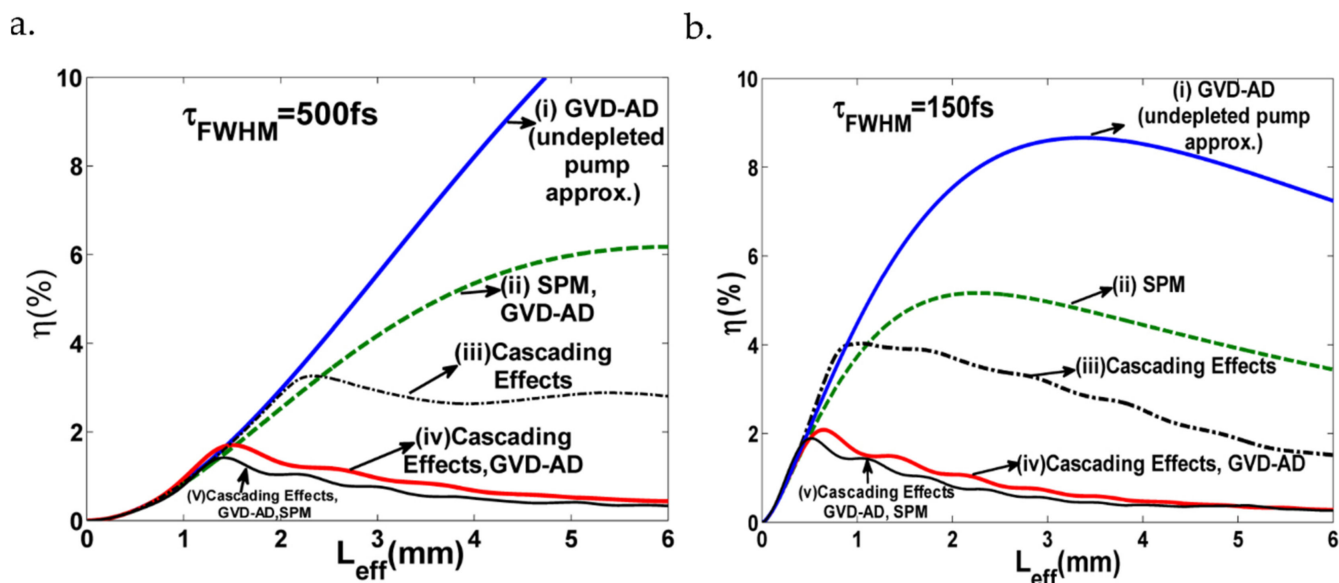


Figure 4. The relation between energy conversion efficiency and effective length when the model includes different effects. Most of the reduction in efficiency comes from the GVD-AD, together with the cascading effects for both (a) a long pulse duration of 500 fs with 40 GW/cm² and (b) a shorter pulse of 150 fs with triple peak intensity. [Reprinted/Adapted] with permission from [73] ©The Optical Society.

In many applications requiring intense THz fields, such as matter manipulation, the peak electric or magnetic field are the relevant quantities. Intuitively, the electrical field is inversely proportional to the waist radius at focus. However, the focus radius is limited by the longer characteristic wavelengths in this region. Moreover, due to the asymmetric beam and diffraction, tight focusing becomes more challenging and requires optics with more careful design. As reported by Hirori et al. [29], THz generation through the use of a 4f-grating-telescope setup has a near-collimated beam with diffraction-limited divergence. In this design, the cross-section of THz related to pump spot size, imaging error, and THz absorption, has an elliptical shape. with mm FWHM. Since the focus spot size is determined by the ratio between the actual beam diameter and the focal length of the focusing mirrors, the narrow spot size of the emitted THz is magnified 10× through a telescope composed of two parabolic mirrors, PM1 and PM2, as shown in Figure 2c. A 3 μJ pulse was generated from a 1 kHz 3 mJ amplifier system with a 0.1% energy conversion efficiency. Using the optics described above, the THz pulse was focused down to a near diffraction-limit spot size of 300 μm at 1 THz, through the use of an off-axis parabolic mirror with an effective f number of 1. The peak electric field was estimated to reach 1.2 MV/cm, which is the record for a kHz system.

4. Discrete TPF

A high groove-density grating produces continuous TPF through angular dispersion. However, this large angular dispersion limits the effective interaction length for optical–THz conversion, distorts the image for short pulses with large spectral bandwidth, and deteriorates the THz beam profile, inhibiting THz generation and its tight focusing. Recently, methods free of angular dispersion have been proposed to minimize these issues [75]. As shown in Figure 5c, a reflective stair-step echelon splits the pump beam into a superposition of beamlets [76]. Instead of tilting the pulse front continuously, the beamlets form a discrete tilted series, each of which radiates a THz wave in a Cherenkov manner. A digital micromirror device (DMD) with electronically controllable micromirror arrays can also provide a commercial and flexible solution to adjust the discrete TPF [77]. As shown in Figure 5a, the beamlets are separated by the transverse distance Δx , and a time delay Δt . The tilt angle γ follows the relation $\gamma = \tan^{-1} \frac{\Delta t \cdot v_g}{\Delta x}$, in which v_g is the group velocity of the

pump pulse in LN. The THz generated from neighboring beamlets interferes constructively only if the transverse distance Δx does not exceed the beam radius σ . The beam radius should be large enough to avoid the strong diffraction of the pump pulse and the generated THz, while a smaller beam radius provides higher THz frequency components [63]. In the absence of angular dispersion, material dispersion, beam divergence, and THz absorption become the key factors that limit THz generation. To reduce the divergence of the pump, in one recent experiment the beamlets formed by echelon were further imaged by a telescope system to improve collimation [76]. The conversion efficiency reached 0.33% at a cryogenic temperature, and a 3.1 μJ THz pulse energy with 500 kV/cm peak field was demonstrated with a 1 kHz repetition rate, a 70 fs pulse duration, and 0.95 mJ pulse energy [76].

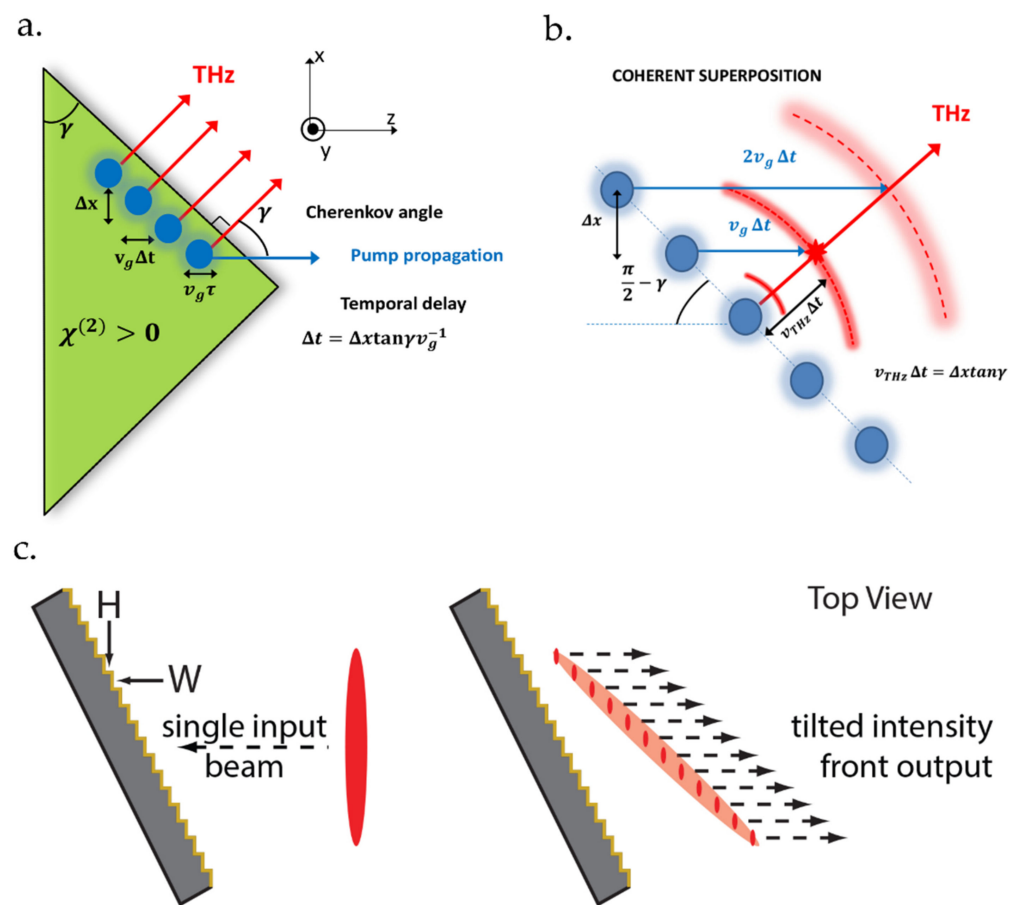


Figure 5. Phase matching condition for beamlet superposition and methods to generate a discrete TPF. (a) The beamlets have a pulse duration τ , transverse separation distance Δx , and delay between beamlets Δt . (b) The superposition of the neighboring beamlets exists if $\Delta x < \sigma$. The strong divergence prevents the superposition with further beamlets. (c) When the pump laser is incident on the reflective echelon, the beamlets are generated with a discrete TPF. The height H and width W of the echelon steps give the tilt angle $\theta = \tan^{-1} \frac{2H}{W}$. Considering the demagnification factor M of the lenses and the refractive index n_{NIR}^{gr} of LN, the tilt angle in the crystal further becomes $\gamma = \tan^{-1} \frac{2HM}{Wn_{NIR}^{gr}}$. [Reprinted/Adapted] with permission from [75,76], ©The Optical Society.

Hybrid-type setups which tilt the pulse front in two stages have also been proposed to combine the advantages of different techniques. The concept of combining transmission and contact gratings was initially proposed to lower the requirement for high-groove contact grating and maintain the advantage of reducing imaging errors [78]. In addition, as shown in Figure 6a, since the THz radiation needs to leave the surface perpendicularly, the wedge angle δ follows the relation $\delta = \gamma - \theta_{d2}$, where γ is the tilt angle for phase matching and θ_{d2} is the diffracted angle by contact grating. The optimized δ is reduced to

$\sim 30^\circ$, smaller than the angle ($\sim 63^\circ$) in a conventional TPF. A smaller wedge angle is good to accommodate larger pump spot size and improve the THz beam profile [79], since different edges of the THz beam undergo different generation and absorption processes in the prism. We note that it is possible to reduce the wedge angle further by combining the continuous and discrete techniques to generate a TPF [78–80]. As in Figure 6b, a transmission grating and lens are used to pre-tilt the pulse front in air to be parallel with the pump entrance surface. The tilt angle in LN will be reduced by the large group refractive index of the pump, but the LN crystal itself is tailored with an echelon structure (nonlinear echelon slab, NELES), increasing the tilt angle through discrete TPF. A further improvement is to remove the lens after the grating, to be free of imaging errors [81]. These hybrid designs are promising for the generation of a more uniform THz beam profile, which can improve the focus and reach a higher peak field [82].

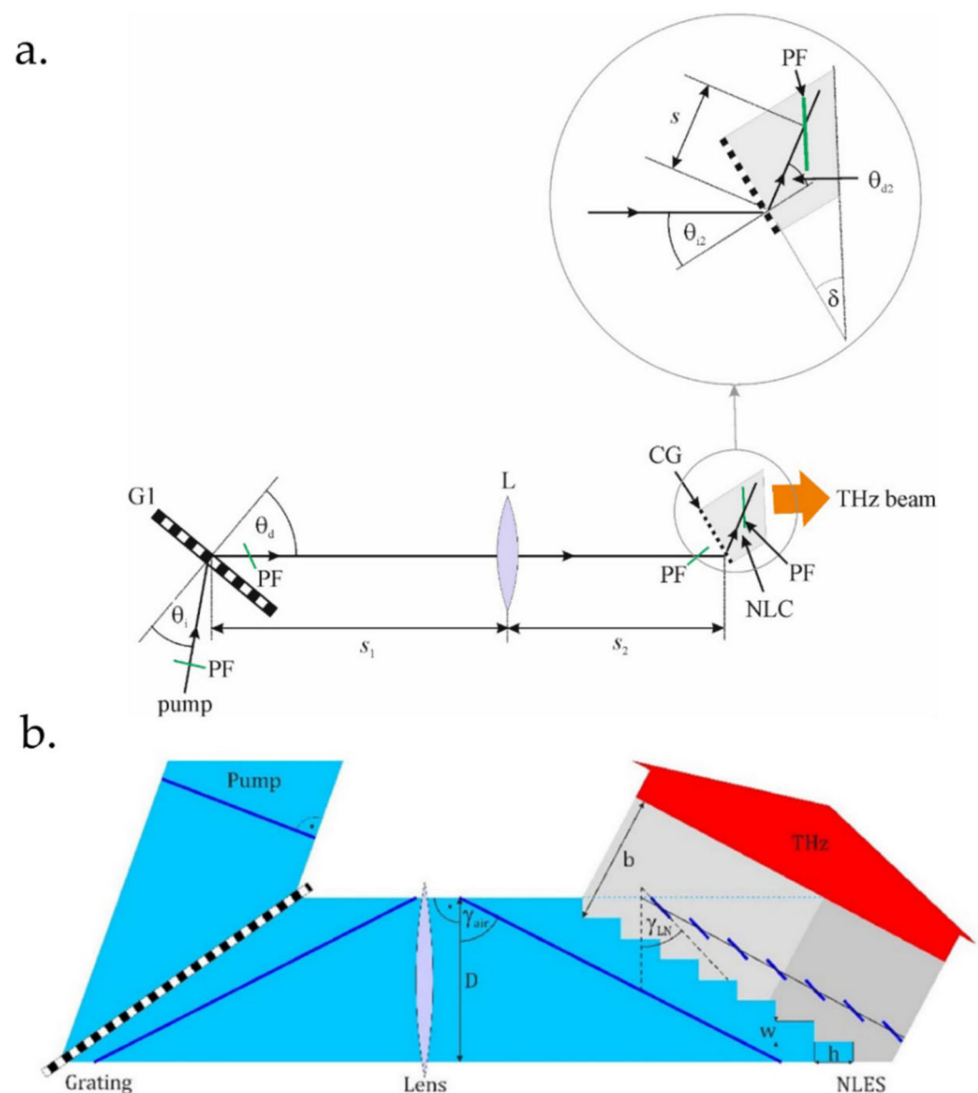


Figure 6. Schematic representation of the hybrid structure. (a) The hybrid structure uses transmission grating and lens and contact grating for TPF. (b) The transmission grating, lens and echelon surface on the LN tilt the pulse front (deep blue line) together. The average TPF in the LN crystal is shown by a grey solid line parallel with the pump incidence surface and the THz emitting surface of the NLES. [Reprinted/Adapted] with permission from [78,80], ©The Optical Society.

The advantages and disadvantages of different techniques of generating single- to few-cycle THz pulses are summarized in Table 1.

Table 1. Comparison of techniques to generate single- to few-cycle THz pulses from LN.

Techniques		Advantages	Disadvantages	Refs	
Cherenkov geometry	Point/line focusing	<ul style="list-style-type: none"> • Compatible with high repetition rate system • High conversion efficiency 	<ul style="list-style-type: none"> • Low excitation power • Divergent THz emission 	[48–59]	
	Continuous TPF	Grating-telescope	<ul style="list-style-type: none"> • Scalable excitation power • One-direction THz emission 	<ul style="list-style-type: none"> • Imaging errors • Short interaction length due to angular dispersion • Non-uniform THz generation 	[26–31,34–44,68–74]
	Tilted pulse front (TPF)	Contact grating	<ul style="list-style-type: none"> • No imaging error 	<ul style="list-style-type: none"> • Low diffraction efficiency • Hard for fabrication 	[63–67]
	Discrete TPF		<ul style="list-style-type: none"> • No angular dispersion • Broad pump bandwidth 	<ul style="list-style-type: none"> • Imaging errors • Non-uniform THz generation 	[75–77]
	Hybrid type		<ul style="list-style-type: none"> • Less imaging errors • Symmetric THz profile 	<ul style="list-style-type: none"> • Lack of parameter flexibility 	[78–82]

5. Conclusions and Prospects

We provided an overview of the methods used to generate intense single- to few-cycle THz radiation from LN crystals. We summarized the various techniques that have been proposed and their optimization to solve phase matching issues, reach high conversion efficiency, and generate high THz-pulse energies. Cherenkov-like radiation techniques provide a means to generate THz with high conversion efficiency but are limited by the small pump area. To scale up the pump pulse energy, the TPF method was developed with an extended pump spot size in two dimensions, but requiring the understanding and fine adjustment of several parameters to achieve optimum phase matching conditions, including imaging errors, dispersion effects, SPM, and cascading effects. In addition, parameters like pulse duration and temperature require optimization to improve generation efficiency and reduce the absorption of THz. Currently, THz pulse energies at the mJ level have been reported from a low-repetition-rate laser with high conversion efficiency. Another key issue to obtain high peak field is the ability to focus the THz beam as close to the diffraction limit as possible. After the optimization of THz generation and focusing, a peak field at the MV/cm level has been demonstrated in a 1 kHz Ti:Sapphire system. More novel techniques, including discrete TPF methods and hybrid structures, have also been developed, with the advantages of lower angular dispersion, less imaging aberration. or more uniform THz generation, opening new avenues to high-field THz.

This field is still developing in several directions. The focusing of high-energy THz pulses to the diffraction limit is still lacking. Ideally, a mJ THz pulse with tight focus would achieve a greater-than 10 MV/cm peak field, but the current peak field record

remains at 6.3 MV/cm from a more than 1 mJ THz pulse [31]. In addition, the discrete TPF method shows great potential to achieve higher conversion efficiency, although the experimental results stay far below those of the theoretical calculation [75]. More complex theoretical models including the cascading effect will be helpful to understand the current discrepancy and limitations. Finally, new configurations and mechanisms to generate THz in LN have recently emerged, such as the quasistatic precursor method [83,84], which shows the possibility of generating an intense THz radiation with a high repetition rate and high average power systems. This will open new avenues for high signal-to-noise nonlinear spectroscopy.

Author Contributions: X.Z., D.R.B., J.M. and K.M.D. contributed to writing and editing this review. X.Z., D.R.B., J.M. and K.M.D. approved the paper. All authors have read and agreed to the published version of the manuscript.

Funding: This work was supported by JSPS KAKENHI Grant number 21K14217 and in part by funding from the Femtosecond Spectroscopy Unit, Okinawa Institute of Science and Technology Graduate University.

Institutional Review Board Statement: Not applicable.

Informed Consent Statement: Not applicable.

Data Availability Statement: Data sharing not applicable.

Acknowledgments: We acknowledge the supports from the Femtosecond Spectroscopy Unit of the Okinawa Institute of Science and Technology Graduate University.

Conflicts of Interest: The authors declare no conflict of interest. The funders had no role in the design of the study; in the collection, analyses, or interpretation of data; in the writing of the manuscript, or in the decision to publish the results.

References

- Leguy, A.M.A.; Goñi, A.R.; Frost, J.M.; Skelton, J.; Brivio, F.; Rodríguez-Martínez, X.; Weber, O.J.; Pallipurath, A.; Alonso, M.I.; Campoy-Quiles, M.; et al. Dynamic disorder, phonon lifetimes, and the assignment of modes to the vibrational spectra of methylammonium lead halide perovskites. *Phys. Chem. Chem. Phys.* **2016**, *18*, 27051–27066. [[CrossRef](#)]
- Steinleitner, P.; Merkl, P.; Nagler, P.; Mornhinweg, J.; Schüller, C.; Korn, T.; Chernikov, A.; Huber, R. Direct Observation of Ultrafast Exciton Formation in a Monolayer of WSe₂. *Nano Lett.* **2017**, *17*, 1455–1460. [[CrossRef](#)]
- La-o-vorakiat, C.; Salim, T.; Kadro, J.; Khuc, M.-T.; Haselsberger, R.; Cheng, L.; Xia, H.; Gurzadyan, G.G.; Su, H.; Lam, Y.M.; et al. Elucidating the role of disorder and free-carrier recombination kinetics in CH₃NH₃PbI₃ perovskite films. *Nat. Commun.* **2015**, *6*, 7903. [[CrossRef](#)]
- Yu, S.; Gao, B.; Kim, J.W.; Cheong, S.-W.; Man, M.K.L.; Madéo, J.; Dani, K.M.; Talbayev, D. High-Temperature Terahertz Optical Diode Effect without Magnetic Order in Polar FeZnMo₃O₈. *Phys. Rev. Lett.* **2018**, *120*, 037601. [[CrossRef](#)] [[PubMed](#)]
- Katayama, I.; Aoki, H.; Takeda, J.; Shimosato, H.; Ashida, M.; Kinjo, R.; Kawayama, I.; Tonouchi, M.; Nagai, M.; Tanaka, K. Ferroelectric Soft Mode in a SrTiO₃ Thin Film Impulsively Driven to the Anharmonic Regime Using Intense Picosecond Terahertz Pulses. *Phys. Rev. Lett.* **2012**, *108*, 097401. [[CrossRef](#)] [[PubMed](#)]
- Kozina, M.; Fechner, M.; Marsik, P.; van Driel, T.; Glownia, J.M.; Bernhard, C.; Radovic, M.; Zhu, D.; Bonetti, S.; Staub, U.; et al. Terahertz-driven phonon upconversion in SrTiO₃. *Nat. Phys.* **2019**, *15*, 387–392. [[CrossRef](#)]
- Li, X.; Qiu, T.; Zhang, J.; Baldini, E.; Lu, J.; Rappe, A.M.; Nelson, K.A. Terahertz field-induced ferroelectricity in quantum paraelectric SrTiO₃. *Science* **2019**, *364*, 1079–1082. [[CrossRef](#)] [[PubMed](#)]
- Yang, X.; Vaswani, C.; Sundahl, C.; Mootz, M.; Gagel, P.; Luo, L.; Kang, J.H.; Orth, P.P.; Perakis, I.E.; Eom, C.B.; et al. Terahertz-light quantum tuning of a metastable emergent phase hidden by superconductivity. *Nat. Mater.* **2018**, *17*, 586–591. [[CrossRef](#)]
- Nanni, E.A.; Huang, W.R.; Hong, K.-H.; Ravi, K.; Fallahi, A.; Moriena, G.; Dwayne Miller, R.J.; Kärtner, F.X. Terahertz-driven linear electron acceleration. *Nat. Commun.* **2015**, *6*, 8486.
- Schubert, O.; Hohenleutner, M.; Langer, F.; Urbanek, B.; Lange, C.; Huttner, U.; Golde, D.; Meier, T.; Kira, M.; Koch, S.W.; et al. Sub-cycle control of terahertz high-harmonic generation by dynamical Bloch oscillations. *Nat. Photonics* **2014**, *8*, 119–123. [[CrossRef](#)]
- Hirori, H.; Shinokita, K.; Shirai, M.; Tani, S.; Kadoya, Y.; Tanaka, K. Extraordinary carrier multiplication gated by a picosecond electric field pulse. *Nat. Commun.* **2011**, *2*, 594. [[CrossRef](#)] [[PubMed](#)]
- Kampfrath, T.; Sell, A.; Klatt, G.; Pashkin, A.; Mährlein, S.; Dekorsy, T.; Wolf, M.; Fiebig, M.; Leitenstorfer, A.; Huber, R. Coherent terahertz control of antiferromagnetic spin waves. *Nat. Photonics* **2010**, *5*, 31. [[CrossRef](#)]
- Cocker, T.L.; Jelic, V.; Gupta, M.; Molesky, S.J.; Burgess, J.A.J.; Reyes, G.D.L.; Titova, L.V.; Tsui, Y.Y.; Freeman, M.R.; Hegmann, F.A. An ultrafast terahertz scanning tunnelling microscope. *Nat. Photonics* **2013**, *7*, 620–625. [[CrossRef](#)]

14. Cocker, T.L.; Peller, D.; Yu, P.; Repp, J.; Huber, R. Tracking the ultrafast motion of a single molecule by femtosecond orbital imaging. *Nature* **2016**, *539*, 263–267. [[CrossRef](#)] [[PubMed](#)]
15. Reimann, J.; Schlauderer, S.; Schmid, C.P.; Langer, F.; Baierl, S.; Kokh, K.A.; Tereshchenko, O.E.; Kimura, A.; Lange, C.; Gdde, J.; et al. Subcycle observation of lightwave-driven Dirac currents in a topological surface band. *Nature* **2018**, *562*, 396–400. [[CrossRef](#)]
16. Fleischer, S.; Field, R.W.; Nelson, K.A. Commensurate Two-Quantum Coherences Induced by Time-Delayed THz Fields. *Phys. Rev. Lett.* **2012**, *109*, 123603. [[CrossRef](#)] [[PubMed](#)]
17. Uchida, K.; Hirori, H.; Aoki, T.; Wolpert, C.; Tamaya, T.; Tanaka, K.; Mochizuki, T.; Kim, C.; Yoshita, M.; Akiyama, H.; et al. Time-resolved observation of coherent excitonic nonlinear response with a table-top narrowband THz pulse wave. *Appl. Phys. Lett.* **2015**, *107*, 221106. [[CrossRef](#)]
18. Matsunaga, R.; Shimano, R. Nonequilibrium BCS State Dynamics Induced by Intense Terahertz Pulses in a Superconducting NbN Film. *Phys. Rev. Lett.* **2012**, *109*, 187002. [[CrossRef](#)]
19. Ropagnol, X.; Khorasaninejad, M.; Raeiszadeh, M.; Safavi-Naeini, S.; Bouvier, M.; Ct, C.Y.; Larame, A.; Reid, M.; Gauthier, M.A.; Ozaki, T. Intense THz Pulses with large ponderomotive potential generated from large aperture photoconductive antennas. *Opt. Express* **2016**, *11*, 11299. [[CrossRef](#)]
20. Flp, J.A.; Polnyi, G.; Monoszlai, B.; Andriukaitis, G.; Balciunas, T.; Pugzlys, A.; Arthur, G.; Baltuska, A.; Hebling, J. Highly efficient scalable monolithic semiconductor terahertz pulse source. *Optica* **2016**, *3*, 1075–1078. [[CrossRef](#)]
21. Shalaby, M.; Hauri, C.P. Demonstration of a low-frequency three-dimensional terahertz bullet with extreme brightness. *Nat. Commun.* **2015**, *6*, 5976. [[CrossRef](#)] [[PubMed](#)]
22. Vicario, C.; Jazbinsek, M.; Ovchinnikov, A.V.; Chefonov, O.V.; Ashitkov, S.I.; Agranat, M.B.; Hauri, C.P. High efficiency THz generation in DSTMS, DAST and OH1 pumped by Cr:forsterite laser. *Opt. Express* **2015**, *23*, 4573–4580. [[CrossRef](#)]
23. Koulouklidis, A.D.; Gollner, C.; Shumakova, V.; Fedorov, V.Y.; Pugzlys, A.; Baltuska, A.; Tzortzakis, S. Observation of extremely efficient terahertz generation from mid-infrared two-color laser filaments. *Nat. Commun.* **2020**, *11*, 292. [[CrossRef](#)] [[PubMed](#)]
24. Oh, T.I.; Yoo, Y.J.; You, Y.S.; Kim, K.Y. Generation of strong terahertz fields exceeding 8 MV/cm at 1 kHz and real-time beam profiling. *Appl. Phys. Lett.* **2014**, *105*, 041103. [[CrossRef](#)]
25. Yang, K.H.; Richards, P.L.; Shen, Y.R. Generation of Far-Infrared Radiation by Picosecond Light Pulses in LiNbO₃. *Appl. Phys. Lett.* **1971**, *19*, 320–323. [[CrossRef](#)]
26. Hebling, J.; Almsi, G.; Kozma, I.Z.; Kuhl, J. Velocity matching by pulse front tilting for large-area THz-pulse generation. *Opt. Express* **2002**, *10*, 1161–1166. [[CrossRef](#)] [[PubMed](#)]
27. Stepanov, A.G.; Hebling, J.; Kuhl, J. Efficient generation of subpicosecond terahertz radiation by phase-matched optical rectification using ultrashort laser pulses with tilted pulse fronts. *Appl. Phys. Lett.* **2003**, *83*, 3000–3002. [[CrossRef](#)]
28. Huang, S.-W.; Granados, E.; Huang, W.R.; Hong, K.-H.; Zapata, L.E.; Krtner, F.X. High conversion efficiency, high energy terahertz pulses by optical rectification in cryogenically cooled lithium niobate. *Opt. Lett.* **2013**, *38*, 796–798. [[CrossRef](#)] [[PubMed](#)]
29. Hirori, H.; Doi, A.; Blanchard, F.; Tanaka, K. Single-cycle terahertz pulses with amplitudes exceeding 1 MV/cm generated by optical rectification in LiNbO₃. *Appl. Phys. Lett.* **2011**, *98*, 091106. [[CrossRef](#)]
30. Flp, J.A.; Ollmann, Z.; Lombosi, C.; Skrobol, C.; Klingebiel, S.; Plfalvi, L.; Krausz, F.; Karsch, S.; Hebling, J. Efficient generation of THz pulses with 0.4 mJ energy. *Opt. Express* **2014**, *22*, 20155–20163. [[CrossRef](#)]
31. Zhang, B.; Ma, Z.; Ma, J.; Wu, X.; Ouyang, C.; Kong, D.; Hong, T.; Wang, X.; Yang, P.; Chen, L.; et al. 1.4-mJ High Energy Terahertz Radiation from Lithium Niobates. *Laser Photonics Rev.* **2021**, *15*, 2000295. [[CrossRef](#)]
32. Junginger, F.; Sell, A.; Schubert, O.; Mayer, B.; Brida, D.; Marangoni, M.; Cerullo, G.; Leitenstorfer, A.; Huber, R. Single-cycle multiterahertz transients with peak fields above 10 MV/cm. *Opt. Lett.* **2010**, *35*, 2645–2647. [[CrossRef](#)]
33. Seifert, T.; Jaiswal, S.; Sajadi, M.; Jakob, G.; Winnerl, S.; Wolf, M.; Klui, M.; Kampfrath, T. Ultrabroadband single-cycle terahertz pulses with peak fields of 300 kV cm⁻¹ from a metallic spintronic emitter. *Appl. Phys. Lett.* **2017**, *110*, 252402. [[CrossRef](#)]
34. Hebling, J.; Stepanov, A.G.; Almsi, G.; Bartal, B.; Kuhl, J. Tunable THz pulse generation by optical rectification of ultrashort laser pulses with tilted pulse fronts. *Appl. Phys. B* **2004**, *78*, 593–599. [[CrossRef](#)]
35. Stepanov, A.G.; Kuhl, J.; Kozma, I.Z.; Riedle, E.; Almsi, G.; Hebling, J. Scaling up the energy of THz pulses created by optical rectification. *Opt. Express* **2005**, *13*, 5762–5768. [[CrossRef](#)] [[PubMed](#)]
36. Zhong, S.-C.; Li, J.; Zhai, Z.-H.; Zhu, L.-G.; Li, J.; Zhou, P.-W.; Zhao, J.-H.; Li, Z.-R. Generation of 0.19-mJ THz pulses in LiNbO₃ driven by 800-nm femtosecond laser. *Opt. Express* **2016**, *24*, 14828–14835. [[CrossRef](#)] [[PubMed](#)]
37. Wu, X.-J.; Ma, J.-L.; Zhang, B.-L.; Chai, S.-S.; Fang, Z.-J.; Xia, C.-Y.; Kong, D.-Y.; Wang, J.-G.; Liu, H.; Zhu, C.-Q.; et al. Highly efficient generation of 0.2 mJ terahertz pulses in lithium niobate at room temperature with sub-50 fs chirped Ti:sapphire laser pulses. *Opt. Express* **2018**, *26*, 7107–7116. [[CrossRef](#)]
38. Stepanov, A.G.; Henin, S.; Petit, Y.; Bonacina, L.; Kasparian, J.; Wolf, J.-P. Mobile source of high-energy single-cycle terahertz pulses. *Appl. Phys. B* **2010**, *101*, 11–14. [[CrossRef](#)]
39. Yeh, K.-L.; Hoffmann, M.C.; Hebling, J.; Nelson, K.A. Generation of 10µJ ultrashort terahertz pulses by optical rectification. *Appl. Phys. Lett.* **2007**, *90*, 171121. [[CrossRef](#)]
40. Huang, W.R.; Huang, S.-W.; Granados, E.; Ravi, K.; Hong, K.-H.; Zapata, L.E.; Krtner, F.X. Highly efficient terahertz pulse generation by optical rectification in stoichiometric and cryo-cooled congruent lithium niobate. *J. Mod. Opt.* **2015**, *62*, 1486–1493. [[CrossRef](#)]

41. Hebling, J.; Yeh, K.-L.; Hoffmann, M.C.; Bartal, B.; Nelson, K.A. Generation of high-power terahertz pulses by tilted-pulse-front excitation and their application possibilities. *J. Opt. Soc. Am. B* **2008**, *25*, B6–B19. [[CrossRef](#)]
42. Fulop, J.A.; Palfalvi, L.; Almási, G.; Hebling, J. Design of high-energy terahertz sources based on optical rectification. *Opt Express* **2010**, *18*, 12311–12327. [[CrossRef](#)]
43. Fülöp, J.A.; Palfalvi, L.; Klingebiel, S.; Almási, G.; Krausz, F.; Karsch, S.; Hebling, J. Generation of sub-mJ terahertz pulses by optical rectification. *Opt. Lett.* **2012**, *37*, 557–559. [[CrossRef](#)]
44. Zhong, S.C.; Zhai, Z.H.; Li, J.; Zhu, L.G.; Li, J.; Meng, K.; Liu, Q.; Du, L.H.; Zhao, J.H.; Li, Z.R. Optimization of terahertz generation from LiNbO₃ under intense laser excitation with the effect of three-photon absorption. *Opt. Express* **2015**, *23*, 31313–31323. [[CrossRef](#)] [[PubMed](#)]
45. Furukawa, Y.; Kitamura, K.; Takekawa, S.; Niwa, K.; Hatano, H. Stoichiometric Mg:LiNbO₃ as an effective material for nonlinear optics. *Opt. Lett.* **1998**, *23*, 1892–1894. [[PubMed](#)]
46. Fontana, M.; Chah, K.; Aillerie, M.; Mouras, R.; Bourson, P. Optical damage resistance in undoped LiNbO₃ crystals. *Opt. Mater.* **2001**, *16*, 111–117. [[CrossRef](#)]
47. Auston, D.H.; Cheung, K.P.; Valdmanis, J.A.; Kleinman, D.A. Cherenkov Radiation from Femtosecond Optical Pulses in Electro-Optic Media. *Phys. Rev. Lett.* **1984**, *53*, 1555–1558. [[CrossRef](#)]
48. Theuer, M.; Torosyan, G.; Rau, C.; Beigang, R.; Maki, K.; Otani, C.; Kawase, K. Efficient generation of Cherenkov-type terahertz radiation from a lithium niobate crystal with a silicon prism output coupler. *Appl. Phys. Lett.* **2006**, *88*, 071122. [[CrossRef](#)]
49. Stepanov, A.G.; Hebling, J.; Kuhl, J. THz generation via optical rectification with ultrashort laser pulse focused to a line. *Appl. Phys. B* **2005**, *81*, 23–26. [[CrossRef](#)]
50. Bakunov, M.I.; Mashkovich, E.A.; Tsarev, M.V.; Gorelov, S.D. Efficient Cherenkov-type terahertz generation in Si-prism-LiNbO₃-slab structure pumped by nanojoule-level ultrashort laser pulses. *Appl. Phys. Lett.* **2012**, *101*, 151102. [[CrossRef](#)]
51. Carnio, B.N.; Shahriar, B.; Hopmann, E.; Elezzabi, A.Y. Excitation mode-dependent terahertz radiation generation from a sub-wavelength Si-SiO₂-LiNbO₃-polymer-Si planar waveguide. *IEEE Trans. Terahertz. Sci. Technol.* **2021**. [[CrossRef](#)]
52. Suizu, K.; Koketsu, K.; Shibuya, T.; Tsutsui, T.; Akiba, T.; Kawase, K. Extremely frequency-widened terahertz wave generation using Cherenkov-type radiation. *Opt. Express* **2009**, *17*, 6676–6681. [[CrossRef](#)]
53. Bodrov, S.B.; Stepanov, A.N.; Bakunov, M.I.; Shishkin, B.V.; Ilyakov, I.E.; Akhmedzhanov, R.A. Highly efficient optical-to-terahertz conversion in a sandwich structure with LiNbO₃ core. *Opt. Express* **2009**, *17*, 1871–1879. [[CrossRef](#)] [[PubMed](#)]
54. Bodrov, S.B.; Bakunov, M.I.; Hangyo, M. Efficient Cherenkov emission of broadband terahertz radiation from an ultrashort laser pulse in a sandwich structure with nonlinear core. *J. Appl. Phys.* **2008**, *104*, 093105. [[CrossRef](#)]
55. Bodrov, S.B.; Ilyakov, I.E.; Shishkin, B.V.; Stepanov, A.N. Efficient terahertz generation by optical rectification in Si-LiNbO₃-air-metal sandwich structure with variable air gap. *Appl. Phys. Lett.* **2012**, *100*, 201114. [[CrossRef](#)]
56. Bakunov, M.I.; Bodrov, S.B. Si-LiNbO₃-air-metal structure for concentrated terahertz emission from ultrashort laser pulses. *Appl. Phys. B* **2010**, *98*, 1–4. [[CrossRef](#)]
57. Bakunov, M.I.; Efimenko, E.S.; Gorelov, S.D.; Abramovsky, N.A.; Bodrov, S.B. Efficient Cherenkov-type optical-to-terahertz converter with terahertz beam combining. *Opt. Lett.* **2020**, *45*, 3533–3536. [[CrossRef](#)]
58. Bodrov, S.B.; Ilyakov, I.E.; Shishkin, B.V.; Bakunov, M.I. Highly efficient Cherenkov-type terahertz generation by 2 μm wavelength ultrashort laser pulses in a prism-coupled LiNbO₃ layer. *Opt. Express* **2019**, *27*, 36059–36065. [[CrossRef](#)]
59. Xu, L.; Zhang, X.C.; Auston, D.H. Terahertz beam generation by femtosecond optical pulses in electro-optic materials. *Appl. Phys. Lett.* **1992**, *61*, 1784–1786. [[CrossRef](#)]
60. Hebling, J. Derivation of the pulse front tilt caused by angular dispersion. *Opt. Quantum Electron.* **1996**, *28*, 1759–1763. [[CrossRef](#)]
61. Stepanov, A.G.; Bonacina, L.; Chekalin, S.V.; Wolf, J.-P. Generation of 30 μJ single-cycle terahertz pulses at 100 Hz repetition rate by optical rectification. *Opt. Lett.* **2008**, *33*, 2497–2499. [[CrossRef](#)] [[PubMed](#)]
62. Kunitski, M.; Richter, M.; Thomson, M.D.; Vredenburg, A.; Wu, J.; Jahnke, T.; Schöffler, M.; Schmidt-Böcking, H.; Roskos, H.G.; Dörner, R. Optimization of single-cycle terahertz generation in LiNbO₃ for sub-50 femtosecond pump pulses. *Opt. Express* **2013**, *21*, 6826–6836. [[CrossRef](#)] [[PubMed](#)]
63. Palfalvi, L.; Fülöp, J.A.; Almási, G.; Hebling, J. Novel setups for extremely high power single-cycle terahertz pulse generation by optical rectification. *Appl. Phys. Lett.* **2008**, *92*, 171107. [[CrossRef](#)]
64. Ollmann, Z.; Hebling, J.; Almási, G. Design of a contact grating setup for mJ-energy THz pulse generation by optical rectification. *Appl. Phys. B* **2012**, *108*, 821–826. [[CrossRef](#)]
65. Tsubouchi, M.; Nagashima, K.; Yoshida, F.; Ochi, Y.; Maruyama, M. Contact grating device with Fabry-Perot resonator for effective terahertz light generation. *Opt. Lett.* **2014**, *39*, 5439–5442. [[CrossRef](#)]
66. Tóth, G.; Palfalvi, L.; Tibai, Z.; Tokodi, L.; Fülöp, J.A.; Márton, Z.; Almási, G.; Hebling, J. Single-cycle scalable terahertz pulse source in reflection geometry. *Opt. Express* **2019**, *27*, 30681–30691. [[CrossRef](#)]
67. Krizsán, G.; Tibai, Z.; Hebling, J.; Palfalvi, L.; Almási, G.; Tóth, G. Lithium niobate and lithium tantalate based scalable terahertz pulse sources in reflection geometry. *Opt. Express* **2020**, *28*, 34320–34327. [[CrossRef](#)]
68. Blanchard, F.; Ropagnol, X.; Hafez, H.; Razavipour, H.; Bolduc, M.; Morandotti, R.; Ozaki, T.; Cooke, D.G. Effect of extreme pump pulse reshaping on intense terahertz emission in lithium niobate at multimillijoule pump energies. *Opt. Lett.* **2014**, *39*, 4333–4336. [[CrossRef](#)]

69. Nagai, M.; Jewariya, M.; Ichikawa, Y.; Ohtake, H.; Sugiura, T.; Uehara, Y.; Tanaka, K. Broadband and high power terahertz pulse generation beyond excitation bandwidth limitation via $\chi(2)$ cascaded processes in LiNbO₃. *Opt. Express* **2009**, *17*, 11543–11549. [[CrossRef](#)]
70. Bodrov, S.B.; Murzanev, A.A.; Sergeev, Y.A.; Malkov, Y.A.; Stepanov, A.N. Terahertz generation by tilted-front laser pulses in weakly and strongly nonlinear regimes. *Appl. Phys. Lett.* **2013**, *103*, 251103. [[CrossRef](#)]
71. Jewariya, M.; Nagai, M.; Tanaka, K. Enhancement of terahertz wave generation by cascaded $\chi(2)$ processes in LiNbO₃. *JOSA B* **2009**, *26*, A101–A106. [[CrossRef](#)]
72. Cronin-Golomb, M. Cascaded nonlinear difference-frequency generation of enhanced terahertz wave production. *Opt. Lett.* **2004**, *29*, 2046–2048. [[CrossRef](#)] [[PubMed](#)]
73. Ravi, K.; Huang, W.R.; Carbajo, S.; Wu, X.; Kärtner, F. Limitations to THz generation by optical rectification using tilted pulse fronts. *Opt. Express* **2014**, *22*, 20239–20251. [[CrossRef](#)]
74. Fülöp, J.A.; Pálfalvi, L.; Hoffmann, M.C.; Hebling, J. Towards generation of mJ-level ultrashort THz pulses by optical rectification. *Opt. Express* **2011**, *19*, 15090–15097. [[CrossRef](#)] [[PubMed](#)]
75. Ravi, K.; Ofori-Okai, B.K.; Nelson, K.A.; Kartner, F.X. Analysis of terahertz generation by beamlet superposition. *Opt. Express* **2019**, *27*, 26547–26568. [[CrossRef](#)]
76. Ofori-Okai, B.K.; Sivarajah, P.; Ronny Huang, W.; Nelson, K.A. THz generation using a reflective stair-step echelon. *Opt. Express* **2016**, *24*, 5057–5068. [[CrossRef](#)] [[PubMed](#)]
77. Murate, K.; Roshtkhari, M.J.; Ropagnol, X.; Blanchard, F. Adaptive spatiotemporal optical pulse front tilt using a digital micromirror device and its terahertz application. *Opt. Lett.* **2018**, *43*, 2090–2093. [[CrossRef](#)] [[PubMed](#)]
78. Pálfalvi, L.; Ollmann, Z.; Tokodi, L.; Hebling, J. Hybrid tilted-pulse-front excitation scheme for efficient generation of high-energy terahertz pulses. *Opt. Express* **2016**, *24*, 8156–8169. [[CrossRef](#)]
79. Pálfalvi, L.; Tóth, G.; Tokodi, L.; Márton, Z.; Fülöp, J.A.; Almási, G.; Hebling, J. Numerical investigation of a scalable setup for efficient terahertz generation using a segmented tilted-pulse-front excitation. *Opt. Express* **2017**, *25*, 29560–29573. [[CrossRef](#)] [[PubMed](#)]
80. Nugraha, P.S.; Krizsán, G.; Lombosi, C.; Pálfalvi, L.; Tóth, G.; Almási, G.; Fülöp, J.A.; Hebling, J. Demonstration of a tilted-pulse-front pumped plane-parallel slab terahertz source. *Opt. Lett.* **2019**, *44*, 1023–1026. [[CrossRef](#)]
81. Tóth, G.; Pálfalvi, L.; Fülöp, J.A.; Krizsán, G.; Matlis, N.H.; Almási, G.; Hebling, J. Numerical investigation of imaging-free terahertz generation setup using segmented tilted-pulse-front excitation. *Opt. Express* **2019**, *27*, 7762–7775. [[CrossRef](#)] [[PubMed](#)]
82. Wang, L.; Toth, G.; Hebling, J.; Kartner, F. Tilted-Pulse-Front Schemes for Terahertz Generation. *Laser Photonics Rev.* **2020**, *14*, 2000021. [[CrossRef](#)]
83. Bakunov, M.I.; Maslov, A.V.; Tsarev, M.V. Optically generated terahertz pulses with strong quasistatic precursors. *Phys. Rev. A* **2017**, *95*, 063817. [[CrossRef](#)]
84. Tsarev, M.V.; Bakunov, M.I. Tilted-pulse-front excitation of strong quasistatic precursors. *Opt. Express* **2019**, *27*, 5154–5164. [[CrossRef](#)] [[PubMed](#)]